JOURNAL OF SYNCHROTRON RADIATION

ISSN: 1600-5775
journals.iucr.org/s

Simultaneous X-ray radioscopy/tomography and energy-dispersive diffraction applied to liquid aluminium alloy foams

Catalina Jiménez, Marlen Paeplow, Paul H. Kamm, Tillmann R. Neu, Manuela Klaus, Guido Wagener, John Banhart, Christoph Genzel and Francisco García-Moreno

J. Synchrotron Rad. (2018). **25**, 1790–1796

JOURNAL OF SYNCHROTRON RADIATION

ISSN 1600-5775

Received 5 December 2017
Accepted 17 August 2018

Edited by A. Momose, Tohoku University, Japan

Keywords: tomography; radioscopy; diffraction; simultaneous; metal foam.

Supporting information: this article has supporting information at journals.iucr.org/s

Simultaneous X-ray radioscopy/tomography and energy-dispersive diffraction applied to liquid aluminium alloy foams

Catalina Jiménez,[a] Marlen Paeplow,[a] Paul H. Kamm,[b] Tillmann R. Neu,[b] Manuela Klaus,[a] Guido Wagener,[a] John Banhart,[b,c] Christoph Genzel[a] and Francisco García-Moreno[b,c]*

[a]Helmholtz-Zentrum Berlin für Materialien und Energie, Albert-Einstein-Strasse 15, Berlin 12489, Germany, [b]Helmholtz-Zentrum Berlin für Materialien und Energie, Hahn-Meitner-Platz 1, Berlin 14109, Germany, and [c]Technische Universität Berlin, Hardenbergstrasse 36, Berlin 10623, Germany.
*Correspondence e-mail: garcia-moreno@helmholtz-berlin.de

High-speed X-ray imaging in two dimensions (radioscopy) and three dimensions (tomography) is combined with fast X-ray diffraction in a new experimental setup at the synchrotron radiation source BESSY II. It allows for *in situ* studies of time-dependent phenomena in complex systems. As a first application, the foaming process of an aluminium alloy was studied in three different experiments. Radioscopy, optical expansion measurements and diffraction were used to correlate the change of foam morphology to the various phases formed during heating of an AlMg15Cu10 alloy to 620°C in the first experiment. Radioscopy was then replaced by tomography. Acquiring tomograms and diffraction data at 2 Hz allows even more details of foam evolution to be captured, for example, bubble size distribution. In a third experiment, 4 Hz tomography yields dynamic insights into fast phenomena in evolving metal foam.

1. Introduction

Fast tomography with a repetition rate of up to 20 Hz using white synchrotron X-rays, so-called four-dimensional or real-time tomography, has been gaining interest recently at different beamlines (Rack *et al.*, 2010; Momose *et al.*, 2011; Takano *et al.*, 2013; Mokso *et al.*, 2015; Maire *et al.*, 2016). Diffraction contrast tomography, or 3DXRD, is also a focus of current research (Hurley *et al.*, 2016; Poulsen, 2012; Ludwig *et al.*, 2014; King *et al.*, 2016). This method allows for a three-dimensional reconstruction of the crystallographic orientation of grains, but owing to long acquisition times it can be applied only to solid and static samples. A system allowing for fast *in situ* tomography and simultaneous diffraction is in high demand, but not many instruments with this capability are available (King *et al.*, 2016; García-Moreno *et al.*, 2013). In cases where structural or morphological changes are correlated with chemical reactions or phase transformations in real time, *e.g.* in the course of temperature variations and in particular for systems out of equilibrium conditions such as foaming of aluminium-based alloys, such experiments are very useful. Our previous work has already demonstrated that this unique option at the multi-purpose experimental EDDI (energy-dispersive diffraction) beamline, synchrotron radiation facility BESSY II, Berlin, is well suited for time-resolved high-temperature *in situ* diffraction experiments combined

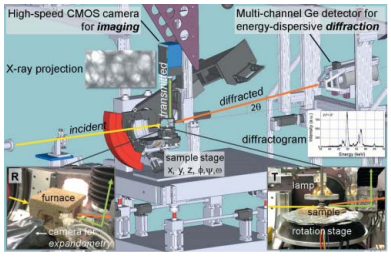

with radioscopy or tomography and simultaneous diffraction at ambient temperature with a time resolution of up to 10 s (0.1 Hz) (García-Moreno *et al.*, 2013).

The recent inclusion of the top-up operation mode (current = 250 mA) at the synchrotron facility BESSY II led to a more constant flux of white X-ray radiation up to ∼120 keV from the superconducting 7 T multipole wiggler at the EDDI beamline. To exploit these new possibilities, a major upgrade of our imaging and diffraction setup was undertaken, which increased its overall performance significantly, *e.g.* increasing the time resolution for tomography by a factor of 40 (to 4 Hz, with 2.5 µm pixel size or larger) and for diffraction by 20 (to 2 Hz). In practice, these values are adapted to the system under study and the data quality required, which leads to a suitable compromise between spatial and time resolution.

In this work we present an *in situ* study of the structural evolution of liquid metal foams and apply up to 4 Hz tomography in combination with up to 2 Hz diffraction. This reveals phase transformations of a foamable aluminium-based alloy and their correlation to the morphological evolution of the foam. The foamable AlMg15Cu10 samples used here do not contain the usual hydrides that release hydrogen and drive bubble formation, but rather contain gas adsorbed to the powder surfaces or dissolved in the intermetallic Al–Mg phases, which induces foaming in the course of heating (Mukherjee *et al.*, 2010). Such foams exhibit near-spherical and closed-cell pores with a near-monomodal size distribution (García-Moreno *et al.*, 2010).

2. Experimental

2.1. Upgraded setup for simultaneous radioscopy/tomography and diffraction

Fig. 1 shows an overview of the instrument and a detailed view of the sample environment. The cross section of the incident beam can be defined by slits up to a maximum field of view of 4 mm × 4 mm. The incoming beam is partially absorbed by the sample, after which a part of the beam is transmitted to the scintillator (green) and another part is diffracted (orange).

The section of the diffracted beam, defined by a secondary slit system, is detected by a multi-channel Ge detector (Canberra model GL0110) that is positioned at a fixed but selectable angle: $2^\circ \leq 2\theta \leq 14^\circ$. Full diffraction patterns were recorded with a repetition rate up to 2 Hz. Further details of the setup were described previously (García-Moreno *et al.*, 2013, 2018). The transmitted beam is converted into visible light by a 200 µm-thick LuAG:Ce scintillator. The image of the X-ray projection is mirrored by 90° upwards, magnified by an optical system by a factor of ∼4.4, and detected by a high-speed DIMAX CMOS camera (2016 pixels × 2016 pixels, 11 µm pixel size) from PCO, Kelheim, Germany. Therefore, each camera pixel corresponds to a sample area of approximately 2.5 µm × 2.5 µm, which gives rise to a measured spatial resolution of 4–5 µm. The image memory of the camera has a size of 36 GB and images a dynamic range of 12 bit. The number of possible images at recording speeds >100 frames s^{-1} depends on the field of view and number of projections used to reconstruct a tomogram. For example, Experiment 2 consists of a sequence of 50 tomograms. The optical path is shielded by 6 mm-thick lead glass (absorption equivalent to 1.5 mm Pb metal) to protect the camera electronics from the X-ray radiation. Imaging contrast is created by differences in the X-ray absorption coefficients of different parts of the sample as well as by their thicknesses, but some propagation phase contrast can be achieved by adjusting the distance between the sample and scintillator, although only to a limited extent because of the beam divergence. Two vertical linear-motion stages are used to move the scintillator into the centre of the beam and to fine-focus the camera onto the scintillator screen.

For *in situ* experiments, combining radioscopy with diffraction and optical expandometry (foam expansion calculated from images captured by a video camera), an X-ray

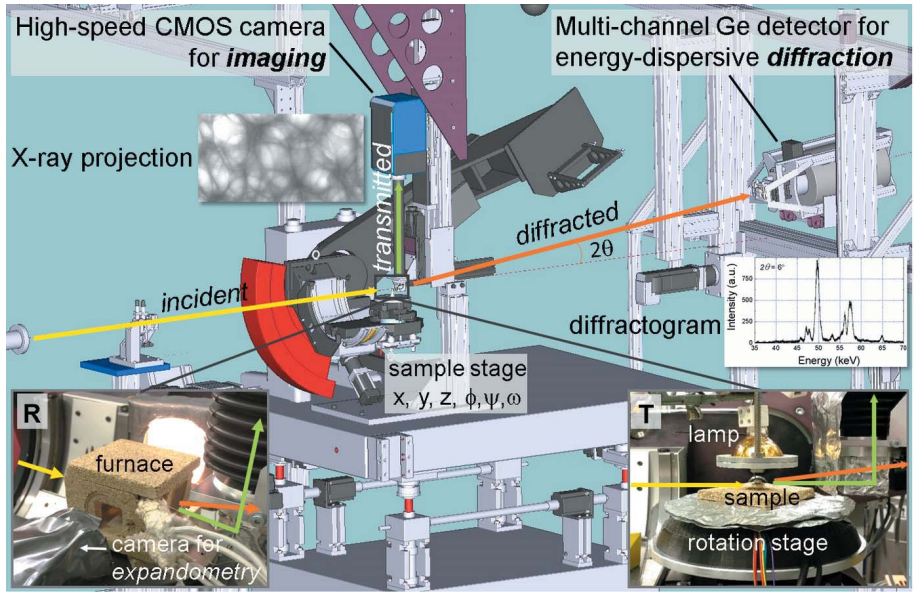

Figure 1
Overview of the upgraded instrumentation at the EDDI beamline with the setup for simultaneous X-ray imaging and energy-dispersive diffraction. The yellow, green and orange arrows depict the incident beam, the transmitted (and reflected) beam and the diffracted signal, respectively. The insets provide photographs of the sample environments mounted on the sample stage for radioscopy (R), consisting of an X-ray-transparent furnace and a camera for expandometry or tomography (T) with a rotation stage right below the beam path and an infrared heating lamp on top. The green arrows in the insets define the path of the transmitted radiation. This beam is transformed into visible light by a scintillator, then mirrored upwards by 90° into the magnifying optic and finally to the high-speed CMOS camera sensor. The orange arrow shows the path of the diffracted beam to the multichannel Ge detector positioned at a fixed but pre-selectable 2θ angle for energy-dispersive diffraction. The outcomes of these experiments are a series of X-ray projection images and diffractograms.

-transparent furnace equipped with a Si_3N_4 ceramic heating plate with up to 900 W heating power allows us to heat up samples to a maximum of 1000°C (see Fig. 1: inset R).

For tomography, a M-660.45 rotation stage from PI miCos GmbH, Eschbach, Germany, is used. Its maximum rotation speed is 720° s^{-1}, which allows for 4 tomograms per second to be acquired (each tomogram requiring 180° rotation and 250 projections). A low-profile, 30 mm-thick, *XY*-stage PPX-32, also from PI miCos GmbH, is mounted on top of the rotation stage. It allows for an easy alignment of the sample axis with the rotation axis. As a result of the compact height of the system, it can be mounted onto the four-axis sample-positioning unit from GE Inspection Technologies, previously available at EDDI (Genzel *et al.*, 2007). It has the capability of using all degrees of freedom of a four-circle diffractometer (x, y, z, φ, ψ, ω and θ). Through eight sliding contacts, up to seven multi-functional electrical channels with up to 60 V DC and 1 A per contact can be connected. Contactless heating by up to three stationary IR-lamps, each with 150 W power, can provide temperatures of up to 700°C for simultaneous tomography and diffraction. The temperature is measured by a thermocouple placed inside the sample holder, is electrically connected through the sliding contacts and touches the bottom part of the sample. After acquisition of radiograms or tomographic projections, all images are background and flat-field corrected. Tomographic reconstructions can be carried out using software packages such as *Octopus* (NV, Octopus – CT reconstruction software, https://octopusimaging.eu/). Commercial software such as *VGStudio Max*, *Avizo* or *Mavi* are available for qualitative and quantitative three-dimensional-image analyses (Graphics, *VGStudioMAX*: https://www.volumegraphics.com/de/produkte/vgstudio-max.html; FEI, Avizo fire: http://www.fei.com/software/avizo3d/, ITWM, *Mavi*: https://www.itwm.fraunhofer.de/de/abteilungen/bv/produkte-und-leistungen/mavi.html). For the analysis of time-resolved tomography scripts and routines based on open source software such as *ImageJ*, Python and commercial software such as *Matlab* are used to cope with the amount of data that is typically two to three orders of magnitude higher than for single tomograms. Further image processing includes standard filters, such as a three-dimensional median filter, or grey value-based segmentation and watershed transformation. The diffraction data are corrected for: wiggler spectrum, Ge-detector dead-time, X-ray absorption, background. The corrected diffraction data were then fitted with pseudo-Voigt functions in order to determine the energy positions. This analysis of the simultaneously recorded diffraction patterns is carried out using software packages written in *Mathematica* and *Matlab*.

2.2. *In situ* metal-foaming experiments

Foamable AlMg15Cu10 (in wt%) precursors of 4 mm × 4 mm × 2 mm are produced by uniaxial hot-compaction (5 min at 440°C and 300 MPa) of Al, Cu and AlMg50 powders and prepared following the powder metallurgical route described elsewhere (Mukherjee *et al.*, 2010).

The first *in situ* experiment was conducted by combining radioscopy, diffraction and optical expandometry. The sample is heated to 620°C at 40°C min^{-1}, held there for 1 min and then cooled down by turning the heating plates off. The acquisition rates are 1 Hz for radioscopy and optical expandometry, and 0.2 Hz for diffraction. The focus of this experiment is the detection of even faint diffraction lines to assure the right identification of occurring phases as well as the synchronized study of foam structure and expansion *versus* time and temperature.

For a second faster *in situ* experiment, contactless IR heating was applied and tomograms of the foaming sample were obtained in real time simultaneously with the diffraction signal, both at a 2 Hz acquisition rate. The sample was placed onto a steel plate mounted on an alumina tube fixed to the top of the fast rotation stage. The rotation stage is thermally shielded by aluminium foil and vermiculite plates as shown in Fig. 1, inset T. The sample was heated up to 500°C as shown in the curve $T_s(t)$ in Fig. 4. The sample started to foam once the temperature exceeded the threshold known for this method (Yu *et al.*, 1998).

A third kind of experiment consisted of melting the alloy above 545°C and acquiring tomographies at 4 Hz. The aim of these experiments is to follow the evolution of bubble coalescence at 4 Hz, the maximum rotation speed.

3. Results and discussion

3.1. Experiment 1

Fig. 2 displays the diffracted intensities *versus* time (Fig. 2*a*), the lattice parameter of the Al matrix a_{Al} for the sample temperature $T_s(t)$ and the overall foam area expansion in Fig. 2(*b*) calculated from the images shown in Fig. 2(*d*). The internal foam structure appears in the radioscopy images (Fig. 2*c*). The whole sequence of radiograms and area expansion is provided in Video S1 of the supporting information.

The phases identified in the AlMg15Cu10 powder compact during foaming (see Fig. 2*a*) are Al, Cu, binary β-Al_2Mg_3 and ternary S-$CuMgAl_2$, liquid (L) and ternary T-$(Cu_{1-x}Al_x)_{49}Mg_{32}$ (ICSD Database codes are 107779, 53758, 245336, 415062 and 429416, respectively, for the solid phases) (ICSD, 2017). The diffraction pattern of the cubic T-phase is simulated with *FullProf* (Rodríguez-Carvajal, 1993) by replacing Zn with Cu in the isomorphic prototype of the Al–Mg–Zn system and adopting a lattice parameter of 1.453 nm, reported for the Al-Mg-Cu ternary system by Effenberg *et al.* (2005). The ternary Al–Mg–Cu phase diagram provides helpful information to identify phases and transformations occurring under equilibrium conditions for a given composition within a specified temperature range, in this case at ambient pressure. Fig. 3 shows a vertical section of the Al–Mg–Cu phase diagram, the isopleth at 70 wt% Al within the temperature range 400–580°C adapted from the work by Effenberg *et al.* (2005). Our composition, AlMg15Cu10 (*i.e.* 75 wt% Al), translates to AlMg17Cu5 in at% (atomic percentage). As this isopleth

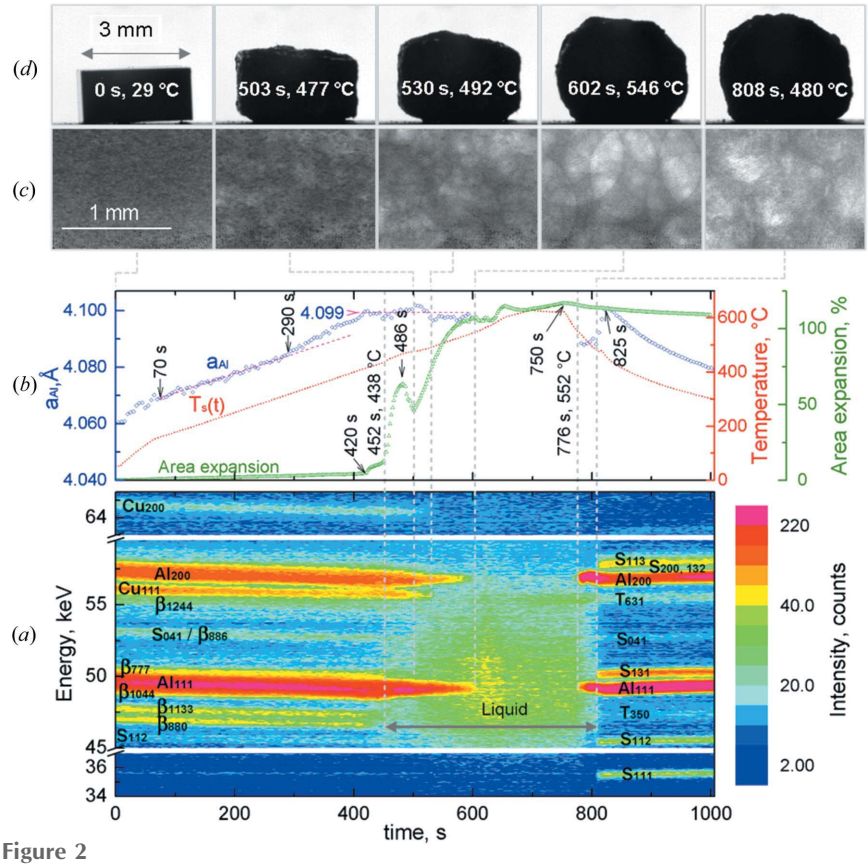

Figure 2
Experiment 1: synchronized *in situ* diffraction, radioscopy and expandometry acquired at 0.5 Hz during foaming of the AlMg15Cu10 alloy at 620°C. (*a*) Map of diffracted intensities *versus* time. Diffraction lines of detected phases Al, Cu, β, S and T are indexed (*hkl*). The presence of liquid in the sample gives rise to diffuse scattering (green zone, broad in energies) and is indicated by an arrow from 452 s to 808 s. (*b*) Sample temperature $T_s(t)$, lattice parameter of the Al matrix a_{Al} and area expansion *versus* time. (*c*) Representative radiograms and (*d*) optical images at times 0, 503, 530, 602 and 808 s showing the foam structure and area expansion, respectively.

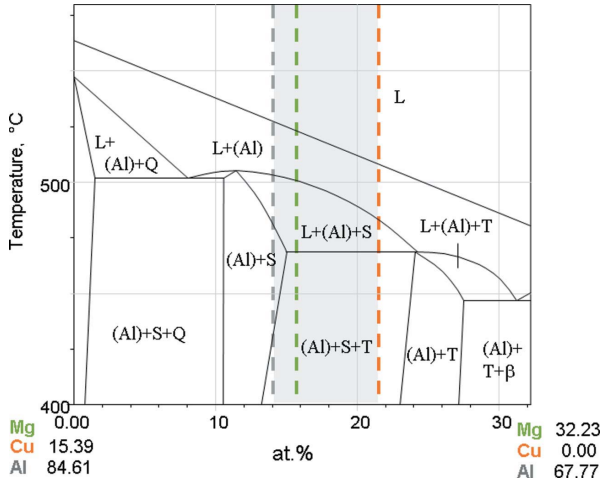

Figure 3
Isopleth at 70 wt% Al of the system Al–Mg–Cu within the temperature range 673–853 K, at ambient pressure (Effenberg *et al.*, 2005). Vertical dashed grey, green and orange lines indicate the Al, Mg and Cu at% contents, respectively, of the nominal alloy AlMg15Cu10 (75 wt% Al), which translates into Al78Mg17Cu5 in at%. As the exact composition of our alloy is not in this isopleth, the colour-coded vertical lines corresponding to each element do not meet but delimit a compositional range denoted by the shaded area in which the occurring phases are Al, S, T and L.

does not contain the exact composition of our alloy, the colour-coded vertical lines corresponding to the content of each element do not meet in a single line. Nevertheless, this compositional range (denoted by the shaded area) is close enough to our real composition to justify the statement that if we had equilibrium conditions the detected phases would be only Al, S, T and L. The judgement 'close enough' can be applied in this case because, upon cooling, we detect only L, Al, T and S phases. But the precursors are made from Al and Cu elemental powders admixed to pre-alloyed AlMg50 (*i.e.* $Al_{12}Mg_{17}$ or γ) that, during hot compaction at 440°C, transform to β and S phases. Thus, before foaming, the phase composition of the precursor is certainly out of equilibrium. This is the main reason for the phase-transformation sequence during heating to differ substantially from predictions based on the Al–Mg–Cu ternary equilibrium phase diagram, and also why we have to determine the phase transformations *in situ* experimentally.

The phase transformations detected by diffraction until the precursor fully melts upon heating and holding are

$$\mathrm{Al + Cu + \beta + S} \xrightarrow[452\,\mathrm{s}]{438^\circ\mathrm{C}} \mathrm{Al + Cu + S + L} \xrightarrow[503\,\mathrm{s}]{477^\circ\mathrm{C}} \mathrm{Al + Cu + L} \xrightarrow[530\,\mathrm{s}]{492^\circ\mathrm{C}} \mathrm{Al + L} \xrightarrow[602\,\mathrm{s}]{546^\circ\mathrm{C}} \mathrm{L}. \quad (1)$$

Cooling starts after 750 s and the detected phase transformations are

$$\mathrm{L} \xrightarrow[776\,\mathrm{s}]{552^\circ\mathrm{C}} \mathrm{L + Al} \xrightarrow[808\,\mathrm{s}]{480^\circ\mathrm{C}} \mathrm{Al + S + T}. \quad (2)$$

The phase transformations during cooling differ in temperature from the phase diagram, with a composition not located in the L + Al + S field before reaching the Al + S + T field, but are in better agreement than the sequence of transformations that occur upon heating, see Fig. 3 (Effenberg *et al.*, 2005).

The lattice parameter of the Al matrix, a_{Al} (Fig. 2*b*), as calculated by sequential fitting of the principal line Al_{111}, allows one to determine the interplanar spacing according to $d_{111} = hc/(2 \sin\theta\, E_{111})$. This is Bragg's law formulated for the energy-dispersive mode, with Planck's constant h and the speed of light c (Genzel *et al.*, 2007). In the course of temperature increase, a_{Al} follows the behaviour of $T_s(t)$. Between 70 s and 290 s, *i.e.* 126°C and 285°C, respectively, a_{Al} expands linearly by 0.388%, which corresponds to a thermal expansion coefficient of $\alpha = 24.4 \times 10^{-6}\ \mathrm{K}^{-1}$. This is slightly above the nominal value of $\alpha_{Al} = 23.1 \times 10^{-6}\ \mathrm{K}^{-1}$. After 292 s,

the slope of a_{Al} exceeds the expected thermal expansion owing to the additional effect of Mg and Cu uptake into the solid solution. From 420 s, a_{Al} no longer expands but oscillates around 4.099 Å as a series of phase transformations occur. Foaming starts at 420 s (415°C), manifested by the loss of linearity of the area-expansion curve caused by the formation of cracks that appear bright in the radiograms (Fig. 2*c*), while the diffraction lines of β undergo a rapid loss of intensity (Fig. 2*a*). At 452 s (438°C) the β lines disappear while diffuse scattering increases, indicating that β melts. The formation of this first liquid heals the cracks so that the gas that formerly was in β starts nucleating in bubbles and foam expansion rises, peaking locally at 486 s (Fig. 2*b*). At 503 s, foam area expansion reaches a local minimum and the intensity of the Cu diffraction lines start to decline, whereas the amount of liquid increases prominently. After 530 s (477°C), when Cu dissolves, the foam expands steadily and former cracks round off to bubbles and expand, but the foam is still in the semi-solid state. At 602 s (546°C), the diffraction lines of Al disappear, *i.e.* the alloy is fully liquid. As the temperature still increases, the foam keeps on expanding. A maximum expansion of 117% is reached after 750 s when cooling starts. The structure seen in the radiogram is not exactly retained upon cooling and solidification after 776 s. The phases S and T form exothermically after 808 s as can be noted from the temporary temperature and lattice parameter increase at 825 s, after which a_{Al} and $T_s(t)$ decrease again. The foam area shrinks by 7% upon cooling so that the final expansion is 110% at 300°C.

Larger maximal area expansions of the order of ~200% have been reported for AlMg15Cu10 (Mukherjee *et al.*, 2010), but only by heating much faster within 30 s from ambient temperature to 600°C in order to prevent loss of the gas liberated from the AlMg50 powder. When heating at 40°C min^{-1}, as in our experiment, 700 s are needed to reach 600°C and some gas is lost during that period. The aim of this experiment is to identify all phase transformations and correlate them with definite expansion regimes. For this we need good temperature resolution and good quality diffraction data, which is why it is necessary to heat slower and count longer.

Some deviations from the expected phase transformations during cooling could be caused by Mg losses since it was reported that long holding periods at 600°C result in heavy oxidation of Mg that gives rise to oxidized outer surfaces (Mukherjee *et al.*, 2010).

3.2. Experiment 2

To remove the above-mentioned limitations, a faster heating cycle is applied to the AlMg15Cu10 precursors during an *in situ* tomography experiment combined with *in situ* diffraction (Fig. 4) up to 500°C. In the tomography imaging mode, we proceed without the optical expansion information but gain information about the three-dimensional evolution of the structure. At 500°C the sample was held in the semi-solid state [melting is completed above 546°C as follows from Fig. 2(*a*)] to prevent Mg losses and too many bubble ruptures that would hinder tomographic reconstruction because of motion artefacts.

Fig. 4(*a*) shows that the phase-transformation sequence on heating and holding is

$$\mathrm{Al + Cu + \beta + S} \xrightarrow[152\ \mathrm{s}]{445^\circ\mathrm{C}} \mathrm{Al + Cu + S + L} \xrightarrow[192\ \mathrm{s}]{491^\circ\mathrm{C}} \mathrm{Al + Cu + L} \xrightarrow[205\ \mathrm{s}]{493^\circ\mathrm{C}} \mathrm{Al + L}. \quad (3)$$

On cooling, the phase transformations are all in agreement with the phase diagram (see Fig. 3),

$$\mathrm{L + Al} \xrightarrow[241\ \mathrm{s}]{465^\circ\mathrm{C}} \mathrm{L + Al + S} \xrightarrow[252\ \mathrm{s}]{426^\circ\mathrm{C}} \mathrm{Al + S + T}. \quad (4)$$

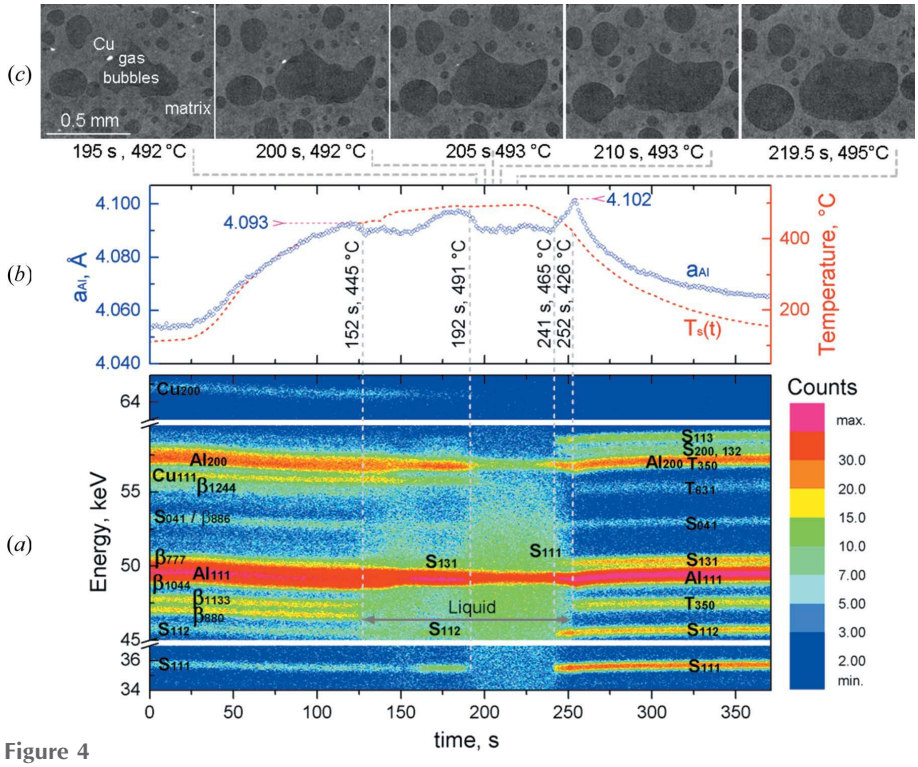

Figure 4
Experiment 2: *in situ* diffraction acquired at 2 Hz during foaming of AlMg15Cu10 at 500°C plus *in situ* tomography also acquired at 2 Hz in the time interval 195–220 s. (*a*) Map of diffracted intensities *versus* time. Diffraction lines of detected phases Al, Cu, β, S and T are indexed (*hkl*). The presence of liquid in the sample gives rise to diffuse scattering (green zone, broad in energies) and is indicated by an arrow from 152 s to 252 s. (*b*) Sample temperature $T_s(t)$ and lattice parameter of the Al matrix a_{Al}. (*c*) Reconstructed slices of the tomographic volume showing the microstructure of the foam at the given times and temperatures. As indicated, the bright small regions are Cu particles that vanish after 205 s, the dark zones are gas bubbles and the dark grey zones represent the semi-molten matrix.

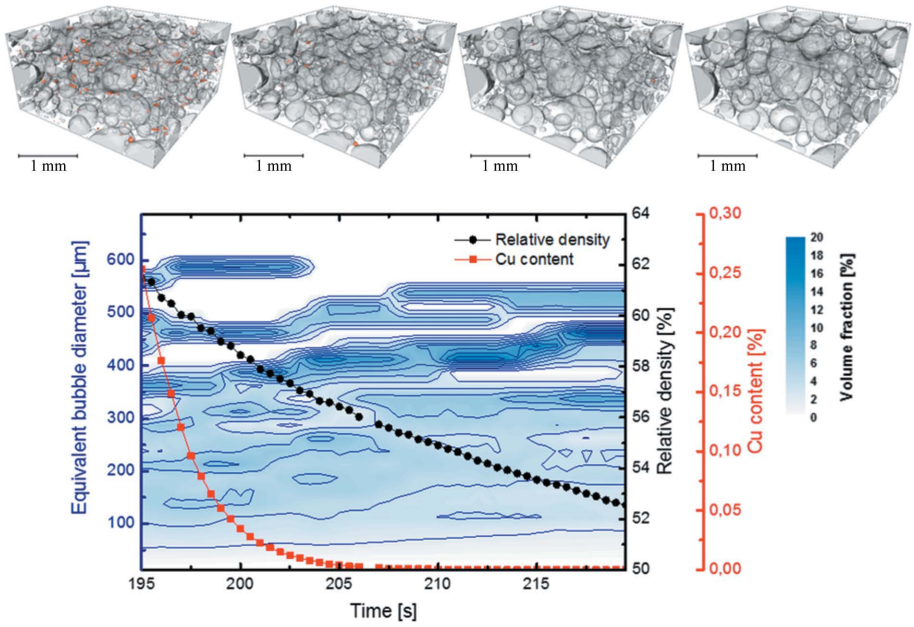

Figure 5
Experiment 2: quantitative three-dimensional analysis of the tomographic *in situ* data from 195 s to 220 s showing the evolution in time of the Cu content, the relative density of the foam and the distribution of equivalent bubble diameters. Selected tomographic reconstructions at 195 s, 200 s, 205 s and 219.5 s show the spatial distributions of Cu particles or Cu-rich zones and gas bubbles.

The lattice parameter of the Al matrix a_{Al} given in Fig. 4(*b*) again follows the temperature $T_s(t)$ except for lattice contractions upon melting or when the S phase precipitates exothermally and a_{Al} increases. The fading of Cu after 205 s is seen in tomographic reconstructions (see Fig. 4*c* and Video S2 of the supporting information). The corresponding quantitative three-dimensional analysis is given in Fig. 5. It is the one order of magnitude larger X-ray attenuation coefficient of Cu compared with those of Al and Mg in the energy range provided by the 7 T multipole wiggler that makes imaging more sensitive than diffraction in the case where the Cu particles are larger than the spatial resolution of the imaging setup. This allows us to detect such a small fraction of Cu and their positions, whereas the principal Cu_{111} diffraction line fades already after 195 s (see Fig. S1 of the supporting information). Most of the enduring Cu particles or Cu-rich zones are larger and closer to bubble surfaces and therefore need the additional 10 s (195–205 s) to dissolve compared with smaller particles fully embedded in the Al matrix.

The evolution of relative foam density and pore size distribution is also given in Fig. 5 within the period from 195 s to 220 s along with representative tomograms showing spatial distributions of Cu and gas bubbles at various times. As Cu dissolves, the liquid fraction increases [see increased diffuse scattering in Fig. 4(*a*) and how gas bubbles tend to become rounded, Fig. 4(*c*)], the foam expands and the relative density decreases by about 10%, while the volume-weighted bubble size distribution (determined from the equivalent diameters of the bubbles located completely inside the considered volume) does not shift significantly to higher values being dominated by bubbles of ~450 µm in size while the number of small bubbles decreases (see Fig. 5). Round submillimetre-sized pores (Mukherjee *et al.*, 2009) and modest expansions as the blowing gas originates from uniformly distributed AlMg50 powder particles (Mukherjee *et al.*, 2010) are typical for this alloy. Besides, Mg disrupts the Al_2O_3 layer covering the Al particles and in this way helps to consolidate the matrix during powder pressing (Shirzadi *et al.*, 2001). The large fraction of AlMg50 powder also provides a measurable liquid fraction already from 445°C during heating. This reduces crack formation in early stages of foaming and prevents gas loss. A temperature of 445°C is significantly lower than the solidus temperatures of other ternary alloys used for foaming such as AlSi6Cu4 (525°C) or AlSiMg4 (548°C) (Helwig *et al.*, 2011).

3.3. Experiment 3

Fig. 6 demonstrates the possibility of analysing fast phenomena such as film ruptures, bubble movement, bubble rearrangements and evolution in detail by 4 Hz tomography *in situ*, *i.e.* at temperatures above 545°C where the alloy is fully liquid. The red and orange marks highlight bubble coalescence and the black circles indicate the motion of small bubbles

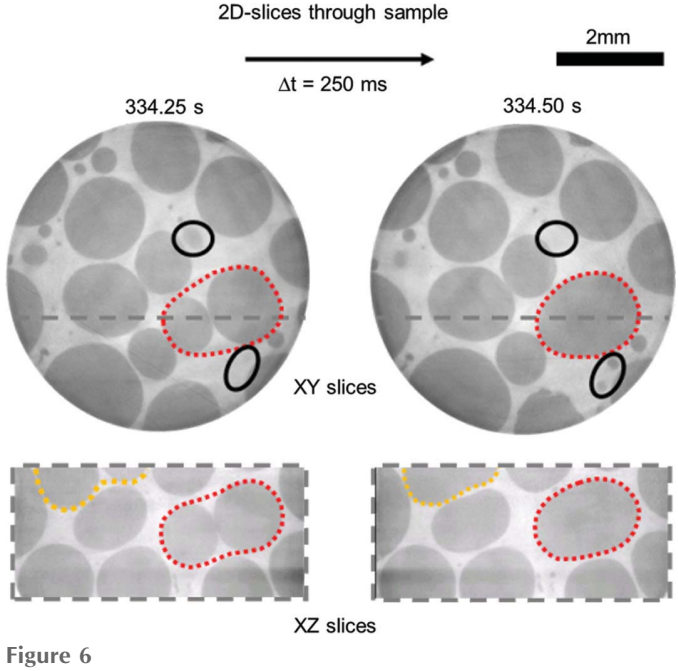

Figure 6
Experiment 3: slices obtained by *in situ* tomography recorded at 4 Hz showing the evolution of the internal structure of AlMg15Cu10 foam above 545°C, allowing us to resolve and follow fast changes of features such as film ruptures and bubble rearrangements in detail. The red and orange marks show the coalescence of two large bubble pairs and the black circles show the disappearance or motion of small bubbles within 250 ms.

within a very short period of time, namely 250 ms. These events are possibly correlated. For a more detailed analysis, an even faster acquisition rate might be required.

4. Conclusions

After a recent upgrade of the EDDI beamline at the BESSY II synchrotron radiation facility, fast tomography experiments with acquisition rates of up to 4 Hz combined with simultaneous diffraction experiments up to 2 Hz repetition frequency can be carried out. This is demonstrated by studying an aluminium alloy foam during foaming and quantifying the interdependence between foam expansion, macrostructure development and the phase transformations occurring during the melting and foaming of a sample.

Funding information

Funding by the European Space Agency (project AO-99-075) and Deutsche Forschungsgemeinschaft (projects BA 1170/35-1 and GA 1304/5-1) is gratefully acknowledged.

References

Effenberg, G., Prince, A., Lebrun, N., Lukas, H. L. & Harmelin, M. G. (2005). *Light Metal Systems*, Part 2, edited by G. Effenberg & S. Ilyenko, pp. 47–78. Berlin, Heidelberg: Springer Verlag.

García-Moreno, F., Jiménez, C., Kamm, P. H., Klaus, M., Wagener, G., Banhart, J. & Genzel, C. (2013). *J. Synchrotron Rad.* **20**, 809–810.

García-Moreno, F., Kamm, P. H., Neu, T. R. & Banhart, J. (2018). *J. Synchrotron Rad.* **25**, 1505–1508.

García-Moreno, F., Mukherjee, M., Solórzano, E. & Banhart, J. (2010). *Int. J. Mater. Res.* **101**, 1134–1139.

Genzel, C., Denks, I. A., Gibmeier, J., Klaus, M. & Wagener, G. (2007). *Nucl. Instrum. Methods Phys. Res. A*, **578**, 23–33.

Helwig, H. M., Garcia-Moreno, F. & Banhart, J. (2011). *J. Mater. Sci.* **46**, 5227–5236.

Hurley, R. C., Hall, S. A., Andrade, J. E. & Wright, J. (2016). *Phys. Rev. Lett.* **117**, 098005.

ICSD (2017). ICSD is available at FIZ Karlsruhe at http://www.fiz-karlsruhe.de/icsd.html or http://icsdweb.fiz-karlsruhe.de.

King, A., Guignot, N., Zerbino, P., Boulard, E., Desjardins, K., Bordessoule, M., Leclerq, N., Le, S., Renaud, G., Cerato, M., Bornert, M., Lenoir, N., Delzon, S., Perrillat, J.-P., Legodec, Y. & Itié, J.-P. (2016). *Rev. Sci. Instrum.* **87**, 093704.

Ludwig, W., King, A. & Reischig, P. (2014). *Strain and Dislocation Gradients from Diffraction*, edited by R. I. Barabash & G. E. Ice, p. 455. London: Imperial College Press.

Maire, E., Le Bourlot, C., Adrien, J., Mortensen, A. & Mokso, R. (2016). *Int. J. Fract.* **200**, 3–12.

Mokso, R., Schwyn, D. A., Walker, S. M., Doube, M., Wicklein, M., Müller, T., Stampanoni, M., Taylor, G. K. & Krapp, H. G. (2015). *Sci. Rep.* **5**, 8727.

Momose, A., Yashiro, W., Harasse, S. & Kuwabara, H. (2011). *Opt. Express*, **19**, 8423–8432.

Mukherjee, M., Garcia-Moreno, F., Jiménez, C. & Banhart, J. (2010). *Adv. Eng. Mater.* **12**, 472–477.

Mukherjee, M., Jiménez, C., Garcia-Moreno, F. & Banhart, J. (2009). German Patent: DE 10 2009 020 004 A1.

Poulsen, H. F. (2012). *J. Appl. Cryst.* **45**, 1084–1097.

Rack, A., Garcia-Moreno, F., Schmitt, C., Betz, O., Cecilia, A., Ershov, A., Rack, T., Banhart, J. & Zabler, S. (2010). *J. X-ray Sci. Technol.* **18**, 429–441.

Rodríguez-Carvajal, J. (1993). *Physica B*, **192**, 55–69.

Shirzadi, A. A., Assadi, H. & Wallach, E. R. (2001). *Surf. Interface Anal.* **31**, 609–618.

Takano, H., Morikawa, M., Konishi, S., Azuma, H., Shimomura, S., Tsusaka, Y., Nakano, S., Kosaka, N., Yamamoto, K. & Kagoshima, Y. (2013). *J. Phys. Conf. Ser.* **463**, 012025.

Yu, C., Eifert, H., Banhart, J. & Baumeister, J. (1998). *Mater. Res. Innov.* **2**, 181–188.